Chemistry–A European Journal

Research Article
doi.org/10.1002/chem.202104426

Chemistry Europe
European Chemical Societies Publishing

www.chemeurj.org

Distinct Bimetallic Cooperativity Among Water Reduction Catalysts Containing [$Co^{III}Co^{III}$], [$Ni^{II}Ni^{II}$], and [$Zn^{II}Zn^{II}$] Cores

Fredricka Morgan,[a] Richard Schaugaard,[a] Dennis Anderson,[a] H. Bernhard Schlegel,*[a] and Cláudio N. Verani*[a]

Dedicated to Professor Ademir Neves (1951–2022), pioneer of bioinorganic chemistry.

Abstract: Three binuclear species $[LCo^{III}_2(\mu\text{-}Pz)_2](ClO_4)_3$ (**1**), $[LNi^{II}_2(CH_3OH)_2Cl_2]ClO_4$ (**2**), and $[LZn^{II}_2Cl_2]PF_6$ (**3**) supported by the deprotonated form of the ligand 2,6-bis[bis(2-pyridylmethyl) amino-methyl]-4-methylphenol were synthesized, structurally characterized as solids and in solution, and had their electrochemical and spectroscopic behavior established. Species **1**–**3** had their water reduction ability studied aiming to interrogate the possible cooperative catalytic activity between two neighboring metal centers. Species **1** and **2** reduced H_2O to H_2 effectively at an applied potential of −1.6 $V_{Ag/AgCl}$, yielding turnover numbers of 2,820 and 2,290, respectively, after 30 minutes. Species **3** lacked activity and was used as a negative control to eliminate the possibility of ligand-based catalysis. Pre- and post-catalytic data gave evidence of the molecular nature of the process within the timeframe of the experiments. Species **1** showed structural, rather than electronic cooperativity, while species **2** displayed no obvious cooperativity. DFT methods complemented the experimental results determining plausible mechanisms.

Introduction

Proton and water reduction with 3d metal-based molecular catalysts yield dihydrogen following a generally accepted[1] sequence of electron/proton transfer steps. It begins with the reduction of a trivalent or divalent 3d metal to reach a low-valent state, for example, $[LM^{I}]^+$. This state becomes nucleophilic to react with a proton and yield a $[LM^{III}\text{-}H^-]^{2+}$ hydride. A second reduction usually takes place to form a more labile $[LM^{II}\text{-}H^-]^+$ hydride, but is not universally observed. If the concentration of protons is low, a homolytic H_2 formation takes place involving two $[LM^{II}\text{-}H^-]^+$ and yielding 2 $[LM^{II}]^+ + H_2$. However, heterolytic H_2 formation is favored when enough protons are available; the hydride $[LM^{II}\text{-}H^-]^+$ reacts directly with the proton H^+ yielding $[LM^{II}\text{-}H_2]^{2+}$. Dihydrogen release and catalyst regeneration, $[LM^{I}]^+ + H_2$ ensues. Depending on factors like the nature of the 3d metal, the ligand framework, the pH of the system, the p_{ka} of $[LM^{III}\text{-}H^-]^{2+}$, competing proton-coupled electron transfer steps take place, and each catalyst will display specific mechanisms. Because the nominal monovalent state $[LM^{I}]^+$ is particularly fragile and can promote undesired ligand reductions leading to the formation of valence tautomer species $[L\bullet M^{II}]$ often associated to deactivation,[2] the design of catalysts containing cooperative metal sites may yield more robust catalysts. Metal cooperativity is pivotal in biological systems[3] and prominent in several catalytic processes.[4] Based on available data, we propose that binuclear cooperativity towards proton/water reduction can be electronic or structural. Electronic cooperativity engages both metal centers on electron transfer, thus shuffling charge and avoiding higher oxidation states or ligand involvement. On the other hand, structural cooperativity happens when the electronic processes are centered on one active site, and no electron transfer takes place among metals, but the second metal serves as a structural reinforcer to avoid catalyst deactivation and decomposition. As such, electronic cooperativity was proposed by Dinolfo et al. [5] for a binuclear Co^{II} catalyst based on a $[N_6O_2]$ Robson-type macrocycle[6] with a Co–Co distance of 3.22 Å. They recently offered a mechanism[7] that involved the reduction and protonation of the $[Co^{II}Co^{II}]$ core yielding a $[Co^{II}Co^{III}\text{-}H]$ hydride, which rearranges into a bridged $[Co^{II}(\mu\text{-}H)Co^{II}]$ hydride core with a Co–Co distance of 3.08 Å. Similarly Qu et al.[8] isolated and characterized a binuclear species supported by benzene-1,2-dithiolate with a [Co(μ-H)Co] core and Co···Co distance of 2.41 Å. They recently investigated other thiolate-bridged [Co(μ-H)Co] species,[1a] however without proposing a detailed mechanism for H_2 formation. We have recently reported on an amido-bridged $[^{LS}Co^{II}(\mu\text{-}N)^{LS}Co^{II}]$ system[9] with a short Co···Co distance of 2.84 Å that catalyzes proton reduction in MeCN. This species displays two aligned but magnetically uncoupled $d_{x2\text{-}y2}$ orbitals in the $[^{LS}Co^{II}\,^{LS}Co^{II}]$ core that enables a consecutive $2e^-$ reduction to yield a $[^{HS}Co^{I}\,^{HS}Co^{I}]$ species. Each of these centers then contributes with $1e^-$ to a single incoming H^+, forming a $[Co^{II}Co^{II}\text{-}H]$ hydride species that precludes formation of an expected $[Co^{I}Co^{III}\text{-}H]$ species.

[a] F. Morgan, Dr. R. Schaugaard, Dr. D. Anderson, Prof. H. B. Schlegel, Prof. C. N. Verani
Department of Chemistry, Wayne State University
5101 Cass Ave., Detroit, MI 48202 (USA)
E-mail: hbs@chem.wayne.edu
claudio.verani@wayne.edu

Supporting information for this article is available on the WWW under https://doi.org/10.1002/chem.202104426

Structural cooperativity seems prevalent in the work by Padhi et al.[10] based on a di(quinolino)pyridine ligand that gave a bridged [Co^{II}(μ-pyridine)Co^{II}] core with Co···Co = 3.13 Å. The group proposed a 1e^- reduction to yield a [$^{HS}Co^{II}Co^{I}$] core with a tetrahedral Co^{I} that forms a five-coordinate hydride in [$^{HS}Co^{II}Co^{III}$-H]. The neighboring ^{HS}Co center remains octahedral along the mechanistic path. A similar system by Papanikolaou et al.[11] included ligand-based reduction with concomitant switch to low spin in both Co^{II} ions. The authors propose that the spin switch modulates the reactivity of the catalytic Co^{II} adding an electronic component to the mostly structural cooperativity.

Studies involving other bimetallic water/proton reduction catalysts are limited; Sakai[12] recently suggested cooperativity on a [$Ni^{II}Ni^{II}$] species based on the lack of activity of the mononuclear counterpart. Not every binuclear catalyst displays cooperativity. Gray et al.[13] evaluated oxime-based Co^{III} catalysts with both flexible hydrocarbon and rigid BO_4 bridges without significant catalytic enhancement. The groups of Nam, Fukuzumi, and Llobet[14] investigated species with pyrazolate and pyridazinate bridges and attributed the lack of cooperativity to factors such as ligand flexibility and Co···Co distances greater than 3.95 Å.

We postulate that (i) close proximity of the metal centers, (ii) the relative coordination environments, and (iii) an appropriate orbital topology are relevant, however, a better understanding of the factors controlling metal cooperativity in H_2 generation remain limited. Similarly, known examples of cooperativity encompass proton reduction and information on the behavior of systems able to reduce water are unknown. Continuing our interest in the mechanisms of proton/water reduction by 3d metal-based catalysts,[15] we study three bimetallic species containing $3d^6$, $3d^8$ and $3d^{10}$ ions, namely, [LCo^{III}_2(μ-Pz)$_2$](ClO$_4$)$_3$ (**1**), [LNi^{II}_2(CH$_3$OH)$_2$Cl$_2$]ClO$_4$ (**2**), and [LZn^{II}_2Cl$_2$]PF$_6$ (**3**), (Figure 1). We establish their solid, solution, and electronic structures, catalytic activity towards water reduction, and ascertain the molecular nature of the process by post-catalytic evaluation. In a concerted experimental/DFT effort we propose mechanisms for cooperativity among two metals

Results and Discussion

Rationale for the catalyst framework

The bicompartmental ligand 2,6-bis[bis(2-pyridylmethyl) amino methyl]-4-methylphenol, HL, is a classic Anderegg pending arm[16] species. It was first described by Suzuki et al.[17] under the name Hbpmp. HL contains a phenol group capable of binding two metal centers at the close proximity of 3 to 4 Å, which are further stabilized by two coordination pockets containing amine and pyridine groups. This [O(NN$'_2$)$_2$] environment can bind to several metals under different oxidation states associated with the water reduction catalytic cycle.[,18b] The metal-metal distance can be controlled by insertion of bridging ligands.

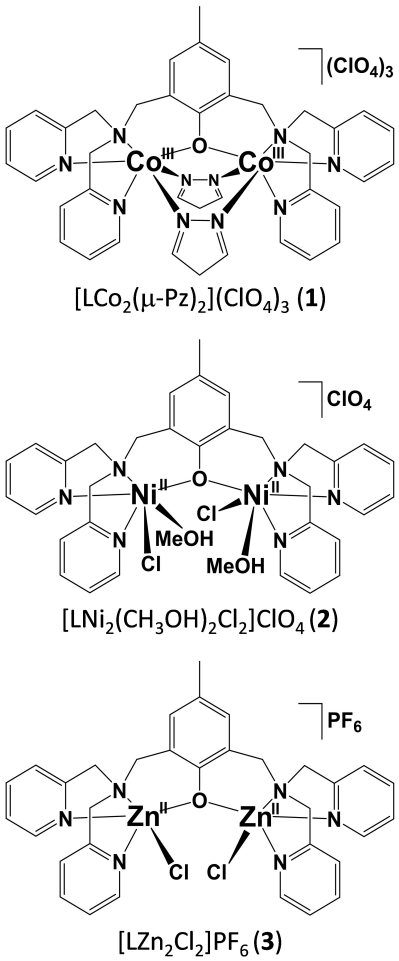

Figure 1. The binuclear complexes **1**, **2**, and **3**.

Syntheses and characterization of 1, 2, and 3

The ligand, HL was synthesized as previously reported.[17,19] Complexes **1**, **2**, and **3** were synthesized by dropwise addition of a methanolic solution of the appropriate metal salt to a methanolic solution of the purified ligand. Compound **1** was treated with excess of pyrazole, which acts both as base to assist phenol deprotonation and bridging ligand, along with hexaaquacobalt(II) perchlorate. Compounds **2** and **3**, were obtained by ligand treatment with the appropriate hexaaquametal chloride salts. All syntheses were performed under aerobic conditions and compounds **2** and **3** were treated respectively with $NaClO_4$ and NH_4PF_6 to yield crystals. These species were thoroughly characterized by 1D and 2D ^{1}H- and ^{13}C NMR, FTIR, and UV-visible spectroscopy, HD-ESI mass spectrometry, cyclic voltammetry. Species **1**–**3** yielded high-quality crystals and their structures were in excellent agreement with the results of combustion analyses. HD-ESI MS results show characteristic peaks at m/z = 260.3981, 779.1319, and 727.0670, respectively for $[1]^{3+}$, $[2]^{+}$, $[3]^{+}$, respectively. There are certain common characteristics exhibited by all three complexes in the FTIR spectra that corroborate with their identities,

namely, a series of strong and medium bands around the 1611–1360 cm^{-1} region attributed to the $\nu_{(C=C)}$ and $\nu_{(C=N)}$ modes of the pyridyl groups.[18b–20] Compounds **1**, and **2** exhibited a sharp peak at 1097 cm^{-1} attributed to the $\nu_{(Cl\text{-}O)}$ mode of the perchlorate counterion, while **3** shows a strong peak at 843 cm^{-1} characteristic of the $\nu_{(PF6)}$ mode for the PF_6^- counterion.

Molecular structures in solid state

$[LCo_2(\mu\text{-}Pz)_2](ClO_4)_3$ (1)

X-ray quality crystals were obtained for **1** through slow evaporation from 4:1 acetonitrile:isopropanol. The molecular structure is shown in Figure 2a and confirms the identity of the main ligand, and the cation being comprised of a binuclear complex cation $[LCo_2(\mu\text{-}Pz)_2]^{3+}$. The environment is completed with three uncoordinated perchlorates. Compound **1** is triclinic and belongs to the $P\bar{1}$ space group (Table S1 in supporting Information). Each Co center is in a pseudo-octahedral geometry and connected to each other by a bridging O^- from the phenolato group. The two metal centers are separated by 3.183 Å, thus relatively shorter distance than as observed in **2** and **3**. This is due to the presence of two bridging pyrazolates bound to the cobalt centers. This feature plays a major role in the cooperativity studies of this compound. Three N-donor atoms, two pyridines and one amine donor, from the 2,6-bis[bis (2-pyridylmethyl) aminomethyl]-4-methylphenol ligand complete the coordination sphere along with two N's from the bridging pyrazolato groups. All Co(1)-N(1,3,5,7, and 9) bond lengths are in the range of 1.933-1.986 Å. The Co(2)-N(2,4,6,8, and 10) bond lengths are in the range of 1.920-1.994 Å. These bond lengths are comparable with the range of Co–N lengths reported in literature.[15f] The Co(1)-O(1), Co(2)-O(1), and Co(1)-O(1)-Co(2) parameters are 1.890 Å, 1.889 Å, and 114.74° respectively. The pioneering work by Chin et al.[21] on homobimetallic cobalt compounds shows Co–N bond lengths ranging between 1.913 and 1.966 Å. Chin et al. also found that Co(1)-O bond lengths were in the range of 1.903–1.959 Å with Co(2)-O bond lengths in the range of 1.885–1.968 Å. The Co–Co distance was 3.529 Å, thus longer than what we found. The differences in these bond lengths arise from the use of phosphate monoesters.[21] The bond angles around each Co center are close to 90° which is an indication of how low spin Co^{III} sites are close to a pseudo-octahedral geometry.[22]

$[LNi_2(CH_3OH)_2Cl_2]ClO_4$ (2)

X-ray quality crystals were obtained for **2** through slow evaporation from methanol. The molecular structure of **2** is shown in Figure 2b and it comprises a binuclear complex cation, $[LNi_2(CH_3OH)_2Cl_2]^+$ balanced by a ClO_4^- counterion. Compound **2** is monoclinic and belongs to the $P2_{1/n}$ space group (Table T1 in Supporting Information). Each nickel center is octahedral, bridged by the phenolate moiety, with two $N_{pyridine}$ and one N_{amine} donor atoms, a methanol, and a chloride completing the hexa-coordinate environment. The two metal centers are separated by 3.953 Å. The Ni(1)-N(1,3,5) bond lengths are in the range of 2.045–2.120 Å and Ni(2)-N(2,4,6) bond lengths are in the range of 2.041 - 2.114 Å. These bond lengths are similar to the reported Ni–N lengths in literature.[15d,18b] The Ni–N bond lengths of our $[Ni^{II}(N_2Py_3)]^{2+}$ [15d] range from 2.024 Å to 2.114 Å. The Ni(1)-Cl(1), Ni(2)-Cl(2), Ni(1)-O(1), Ni(2)-O(1), and Ni(1)-O(1)-Ni(2) parameters are 2.384 Å, 2.382 Å, 2.148 Å, 2.063 Å, and 133.39° respectively. Massoud[18b] observed Ni–N bond distances ranging between 2.042 Å to 2.111 Å. Other bonds are also comparable with Ni–Cl bond lengths ranging from 2.361 Å to 2.3826 Å, Ni–O lengths ranging from 2.069 Å to 2.174 Å and Ni(1)-O–Ni (2) bond angles ranging from 132.6° to 136.63°. These results are comparable to ours.

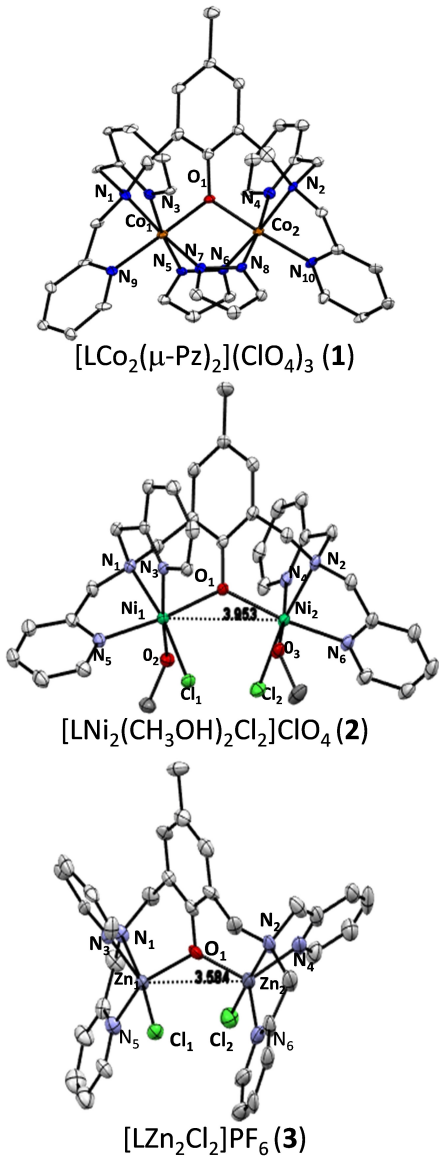

Figure 2. ORTEP representations of the binuclear complexes **1** (CSD 2112779), **2** (CSD 2112780), and **3** (CSD 2112778) at 50% ellipsoid probability. Hydrogen atoms omitted for clarity.

The Ni–Ni distance of 3.953 Å in **2** is longer than the observed metal-metal distance in both **1** and **3**. This is expected for the Pz-bridged **1**, but not for the Zn-containing **3** with a similar framework. This difference is explained by the five coordination of Zn that leads to a distinct orientation of the ligand.

[LZn$_2$Cl$_2$]PF$_6$ (3)

X-ray quality crystals were obtained for **3** through slow evaporation from methanol. The molecular structure of **3** is shown in Figure 2c and comprises a binuclear complex cation, $[LZn_2Cl_2]^+$ and a PF_6^- counterion. Compound **3** is triclinic and belongs to the $P\bar{1}$ space group (Table T2). Each zinc center is pentacoordinated to three N-donor atoms of one bis(2-pyridylmethyl) aminomethyl group, a terminal chloride in the basal site and a bridged phenolate. Zn(1)-N(1,3,5) bond lengths are in the range of 2.064–2.277 Å and Zn(2)-N(2,4,6) bond lengths are in the range of 2.069–2.276 Å. These bond lengths are similar to the reported Zn–N lengths in literature.[18b–23] The Zn(1)-Cl, Zn(2)-Cl, Zn(1)-O(1), Zn(2)-O(1), and Zn(1)-O(1)-Zn(2) parameters are 2.303 Å, 2.284 Å, 2.009 Å, 2.014 Å, and 128.71° respectively. The Zn–Zn distance is 3.584 Å. Studying hydrogen-bond donors as structural and functional models for phosphatase Schenk et al. [23] found the Zn–N and Zn–O bond lengths ranging from 2.144-2.247 Å, and 2.009–2.183 Å respectively. A Zn–O–Zn distance of 3.371 Å was found along with a bond angle of 112.80°. The slight variations of these values result from the presence of two acetate coligands bridging the two zinc centers. Massoud et al.[18b] report a similar range for Zn–N, Zn–O and Zn–Cl bond distances 2.076 Å–2.273 Å, 2.017 Å–2.052 Å and 2.294 Å–2.299 Å respectively with Zn–Zn distance of 3.761 Å and Zn–O–Zn at 135.18°. The variation in Zn–Zn bond distances and Zn–O–Zn angles can be explained by the orientation of the coordinating chloride.

Molecular structures in solution

Proton nuclear magnetic spectra (^{1}H NMR) of compounds **1** and **3** were obtained in acetonitrile (CH_3CN) and dichloromethane (CH_2Cl_2) respectively. Compound **2** is paramagnetic. To confirm the identity of the catalysts in solution as comparable to that in the solid state, multiple 2D NMR[24] methods were used, including correlation spectroscopy (COSY), rotating-frame Overhauser effect spectroscopy (ROESY), and heteronuclear single-quantum correlation spectroscopy (HSQC). COSY is a direct way to show proton coupling. All the peaks on the diagonal correlate to the peaks on the ^{1}H NMR whereas the cross peaks (not on the diagonal) show the coupled protons. Absence of cross peaks implies in lack of coupling. ROESY shows the interaction between non-equivalent protons which are spatially close to each.[25] The cross peaks indicate protons spatially close to each. HSQC experiments determine the correlation between ^{1}H and ^{13}C, with ^{1}H plotted along the X-axis, and ^{13}C along the Y-axis.[26] Correlation between two protons and one carbon provide evidence of asymmetry. Figure 3a-c shows COSY, ROESY and HSQC of 1 in CH_3CN. Full scale ^{1}H NMR of **1** and details of Figures 3a-c are provided in the Supporting Information as Figures S3 to S6, along with a detailed list of peaks. From the COSY spectrum of **1**, the signals at 2.03 ppm (**39**) and 4.27 ppm (**11**, **15**) show no correlation with other peaks, which confirms with the methyl and the aliphatic protons in the ^{1}H NMR spectrum, respectively. The peak at 3.47 ppm (**7′′**,**8′′**) on the other hand is coupled to the peak at 3.64 ppm (**7′**, **8′**), showing the correlation between protons in the aliphatic region (^{1}H NMR spectrum). This correlation is also seen between the two doublet peaks at 4.50 ppm (**13′′**, **17′′**) and 5.17 ppm (**13′**, **17′**). Peaks at 6.85 ppm (**1**, **5**), 7.76 ppm (**20**, **26**, **31**, **37**) and 8.01 ppm (**24**, **33**) shows cross peaks on the COSY spectrum which depicts correlation/coupling, all these signals are seen on the ^{1}H NMR spectrum as pyridyl protons. COSY also shows a correlation between peaks at 8.22 ppm (**22**, **35**) and 8.32 ppm (**25**, **32**) as well as peaks at 7.76 ppm (**20**, **26**, **31**, **37**) and 8.84 ppm (**27**, **30**). These signals are shown as pyridyl protons on the ^{1}H NMR spectrum. The protons on the bridging pyrazoles show at 8.58 ppm (**47**, **50**) which is a singlet and shows on the diagonal of the COSY spectrum with no coupling protons. In a nutshell, the ^{1}H NMR and 2D NMR data confirms that the structure remain unchanged with the solid-state structure of **1**. Full scale ^{1}H NMR signals related to species **3** are shown in Figure S7 along with a detailed list of peaks, whereas Figures S8, S10 and S12 show COSY, ROESY and HSQC for **3** in CH_2Cl_2. Details of Figures S8, S10 and S12 are provided in Figures S9, S11 and S13. In summary, the ^{1}H NMR and 2D NMR data confirm the identity of these species is well preserved as solids and in solution.

Redox and electronic behavior

The cyclic voltammograms of **1**, **2**, and **3** were assessed in MeCN using tetrabutylammonium hexafluoro phosphate ($TBAPF_6$)(0.1 M) as supporting electrolyte and ferrocene as the internal standard.[27] Figure S14 and Table T2 summarize the electrochemical data. In compound **1**, two quasi-reversible metal-based processes are observed: the first process occurs at $E_{1/2} = 0.28\ V_{Ag/AgCl}$ ($-0.12\ V_{Fc/Fc+}$; $\Delta E = 0.14$ V, $|i_{pa}/i_{pc}| = 0.90$) and is attributed to the $Co^{III}Co^{III} \rightarrow Co^{III}Co^{II}$ reduction, while the second process occurs at $E_{1/2} = -0.09\ V_{Ag/AgCl}$ (-0.49 $V_{Fc/Fc+}$; $\Delta E =$ 0.14 V; $|i_{pa}/i_{pc}| = 0.93$). This is attributed to the reduction $Co^{III}Co^{II} \rightarrow Co^{II}Co$.[11,28] An irreversible ligand-based process, possibly associated with phenoxyl formation, is seen around $E_{pa} =$ $1.00\ V_{Ag/AgCl}$ ($0.60\ V_{Fc/Fc+}$). Compound **2** shows an ill-defined reduction process at $E_{1/2} = -0.13\ V_{Ag/AgCl}$ ($-0.52\ V_{Fc/Fc+}$; $\Delta E =$ 0.19 V) and a quasi-reversible process at $E_{1/2} \approx -1.40\ V_{Ag/AgCl}$ ($-1.79\ V_{Fc/Fc+}$; $\Delta E = 0.29$ V), respectively attributed to $Ni^{II}Ni^{II} \rightarrow$ $Ni^{II}Ni^{I}$ and to a nominal $Ni^{II}Ni^{I} \rightarrow Ni^{I}Ni^{I}$.[29] Similar to **1**, a ligand-based process is seen at $E_{1/2} \approx 1.03\ V_{Ag/AgCl}$ ($0.64\ V_{Fc/Fc+}$; $\Delta E =$ 0.08 V. Compound **3** only shows a process at 0.83 $V_{Ag/AgCl}$ ($0.43\ V_{Fc/Fc+}$) also attributed to a phenolate/phenoxyl couple, and similar to the process observed in the unmetallated ligand.[28b] It is unclear why these ligand-based processes display distinct potentials. The limited response of species **3** serves as

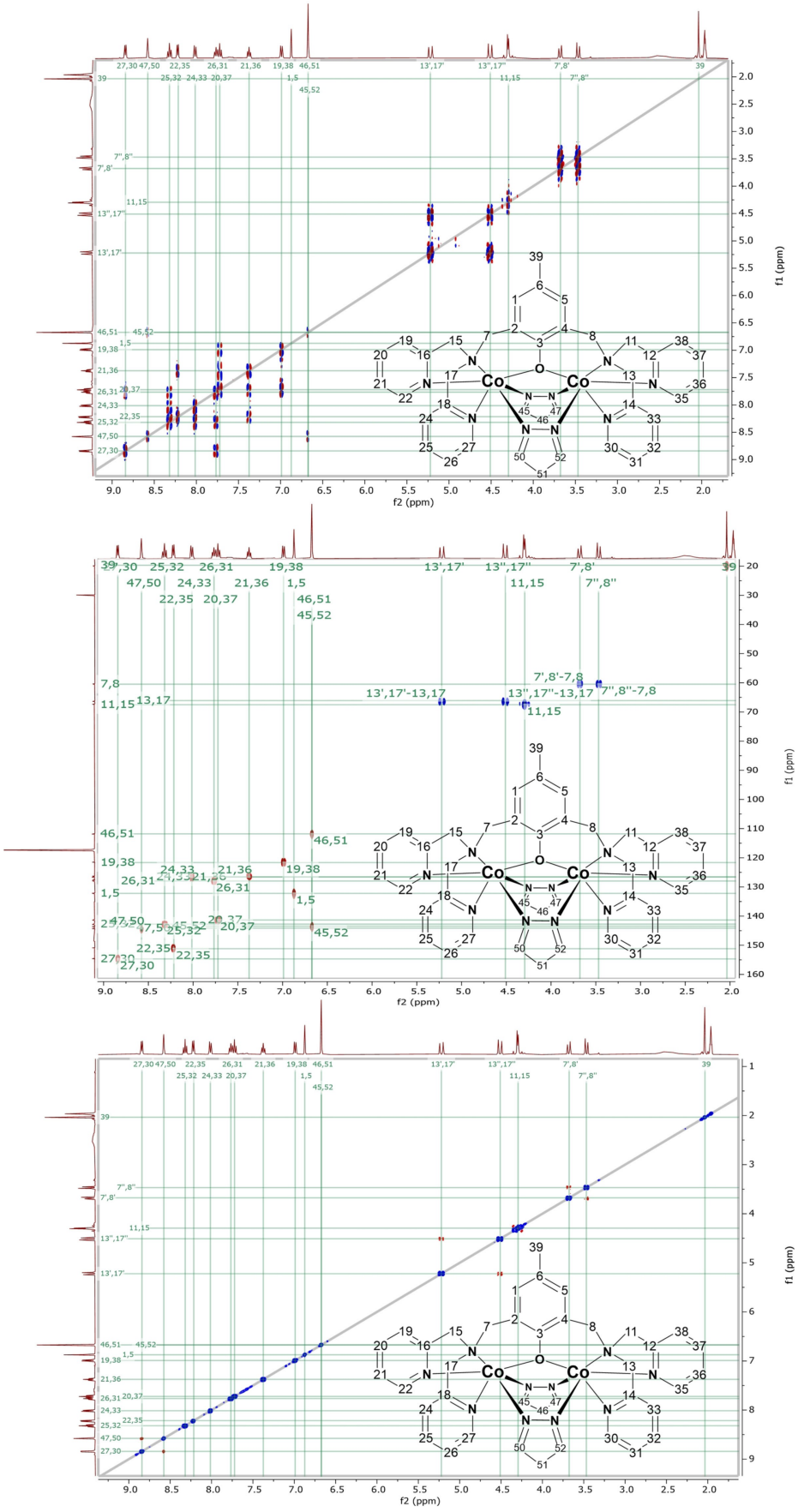

Figure 3. NMR characterization of $[LCo_2(\mu\text{-}Pz)_2](ClO_4)_3$ (**1**): (**a**) COSY, (**b**) ROESY, and (**c**) HSQC spectra in CH_3CN

strong evidence for the need of redox-active metal centers to drive catalysis. For species **1**, the above described MeCN potentials shift ca. 0.20 V on the highly polar phosphate buffer medium used for catalytic experiments (Figure S15). The processes respectively move from 0.28 and −0.09 $V_{Ag/AgCl}$ as broad and ill-defined processes at $E_{pc} \approx 0.04$ and −0.29 $V_{Ag/AgCl}$. A third broad peak is observed at −0.97 $V_{Ag/AgCl}$, thus suggesting that at least one metal center may reach the monovalent state $Co^{II}Co^{II} \rightarrow Co^{II}Co^{I}$ at the catalytic potential. The CVs for species **2** are poorly defined.

The electronic behavior of **1** was assessed in MeCN and showed prominent ultraviolet (UV) bands at 261 nm ($\varepsilon =$ 24,000 $M^{-1}cm^{-1}$) assigned to a ligand-centered π–π* absorption, along with a broad peak at ca. 370 nm ($\varepsilon \approx$4,000 $M^{-1}cm^{-1}$) assigned to a $Co^{III} \leftarrow N_{pyrazole}$ charge transfer transition (LMCT).[30] A less intense absorption is seen at 520 nm (1,003 $M^{-1}cm^{-1}$) attributed to a $Co^{III} \leftarrow$phenolate charge transfer.[28b–31] McKenzie et al.[22] studied a bis-Co^{III} compound with similar electronic features as **1**, however, they assigned the absorption between 390–400 nm to $Co^{III} \leftarrow$phenolate CT.[22] The difference is attributed to distortions caused by distinct phosphate coligands used in that study. The UV-visible of **1** was also measured in phosphate buffer at pH 7. In this spectrum, ligand-centered π–π* absorption, $Co^{III} \leftarrow N_{pyrazole,}$ and $Co^{III} \leftarrow$phenolate charge transfer bands occur at 230 nm ($\varepsilon =$26,000 $M^{-1}cm^{-1}$), 260 nm (sh) ($\varepsilon \approx$1,200 $M^{-1}cm^{-1}$), 380 nm ($\varepsilon =$3,500 $M^{-1}cm^{-1}$), 430 nm (sh) ($\varepsilon =$2,200 $M^{-1}cm^{-1}$), and 520 nm ($\varepsilon =$840 $M^{-1}cm^{-1}$) respectively. Compound **2** exhibits a prominent UV band at 212 nm ($\varepsilon \approx$29,300 $M^{-1}cm^{-1}$) and a shoulder at 257 nm (14,100 $M^{-1}cm^{-1}$) assigned to ligand-centered π-π*. A band at 310 nm (4,100 $M^{-1}cm^{-1}$) is attributed to a phenolate$\leftarrow Ni^{II}$ MLCT and two d-d bands at 585 and 954 nm ($\varepsilon >$ 50 $M^{-1}cm^{-1}$). This is characteristic of a $^{HS}3d^8$ Ni^{II} center in an octahedral geometry with spin-allowed $^3A_{2g} \rightarrow {}^3T_{2g}$ and $^3A_{2g} \rightarrow {}^3T_{1g}$ transitions[32–34] similar to the environment unveiled by X-ray and NMR methods. This observation of **2** is very similar to the findings by Que et al.[35] The UV-visible spectrum of **2** was also measured in phosphate buffer at pH 7. Ligand-centered π–π* absorption and phenolate$\leftarrow Ni^{II}$ MLCT charge transfer bands occur at 211 nm ($\varepsilon =$24,100 $M^{-1}cm^{-1}$), 270 nm (sh) ($\varepsilon =$ 9,500 $M^{-1}cm^{-1}$), and 310 nm ($\varepsilon =$4,530 $M^{-1}cm^{-1}$) respectively. Compound **3** exhibits a prominent UV band at 262 nm ($\varepsilon \approx$ 20,700 $M^{-1}cm^{-1}$) and a shoulder at 292 nm (6,500 $M^{-1}cm^{-1}$) assigned to ligand-centered π-π* transitions.

Behavior as water reduction catalysts

Prior to testing the catalytic activity of **1** and **2** towards water reduction, compounds **1**–**3** were analyzed for proton reduction in CH_3CN in the presence of 0 to 10 equivalents of acetic acid as the proton source. Observed catalytic currents of 174 and 120 μA were respectively measured for **1** and **2** after addition of 10 equivalents of HOAc, with calculated overpotentials of −1.30 and −0.93 V, considering the homoconjugation effect of the acid.[36] (Figure S16). However, the zinc-containing **3** showed no evidence of catalysis after the addition of 10 equivalents of acid. This is a clear indication that **3** is catalytically inert and that catalysis requires the presence of redox-active metal sites such as cobalt and nickel. While the lack of activity in **3** does not preclude ligand involvement in the catalytic cycle, it is a strong indicator that the ligand alone cannot carry catalysis. The electrocatalytic activity of compounds **1** and **2** was then tested towards water reduction in aqueous phosphate buffer at pH of 7, using a mercury pool as working electrode. Negligible amounts of H_2 were produced in the absence of catalysts **1** or **2**, and upon addition of the bimetallic species, catalytic waves were seen at ca. −1.25 $V_{Ag/AgCl}$ (ca. −1.65 $V_{Fc/Fc+}$) for **1** and −1.35 $V_{Ag/AgCl}$ (ca. −1.74 $V_{Fc/Fc+}$) for **2**. (Figure S17) The onset overpotential was calculated at 0.63 V, and 0.73 V for **1**, and **2**, respectively. The thermodynamic potential for H^+ to H_2 was taken as −0.62 $V_{Ag/AgCl}$ in pH 7 aqueous solution.[1c,36] Bulk electrolysis was used to quantify the amount of H_2 generated in **1** (5 μmolL^{-1}), and **2** (6 μmolL^{-1}) at an applied potential of −1.60 V in phosphate buffer (1 M, pH 7) using mercury pool as working electrode, Ag/AgCl as reference electrode and a platinum wire as auxiliary electrode. Under these conditions, the cobalt-containing **1** yielded a turnover number $TON_{30\ min} =$ 2,860 with Faradaic efficiency above 80%. The Ni-containing **2** yielded $TON_{30\ min} =$2,290 with Faradaic efficiency around 95%. The observed Faradaic efficiency suggests that concomitant reactions associated with a decrease in catalytic activity may be operative. Bulk electrolysis experiments in the absence of the catalysts led to an insignificant increase in current. When compounds **1** and **2** were added to the bulk electrolysis system, charge consumption increased significantly. This validates the viability of **1** and **2** as catalysts (Figure 4) within the timeframe of the experiment. Species **1** requires an induction period of about 5 minutes prior to its optimized activity, whereas species **2** seems to consume less charge as time progresses. We tentatively explain these two behaviors as follows: In **1** this induction period coincides with the rearrangement of the catalyst in order to generate at least one five-coordinate catalytic center by means of breaking a Co-$N_{pyrazolate}$ or Co-$N_{pyridine}$; in **2** this is likely associated with deleterious ligand involvement. These results supported our hypothesis of homogeneous water reduction with **1**, and **2** and allowed us to optimize the catalytic conditions based on pH, proceed to post-catalytic analysis, and compare DFT and experimental results in order to propose catalytic pathways.

Dependence of catalytic activity on pH

Species **1** and **2** were probed in phosphate buffers under acidic (pH 6), neutral (pH 7), and basic (pH 8) conditions aiming to optimize their catalytic activity towards water reduction after 30 minutes of bulk electrolysis. Figure 5 shows a plot of TON versus pH for both compounds revealing those acidic conditions lead to TON ≈2,000 for **1** and ~2,100 for **2**. These values are significantly higher than at basic conditions, where TON < 100 for both species and slightly lower than at neutral pH where **1** and **2** have similar TON values of 2,300.

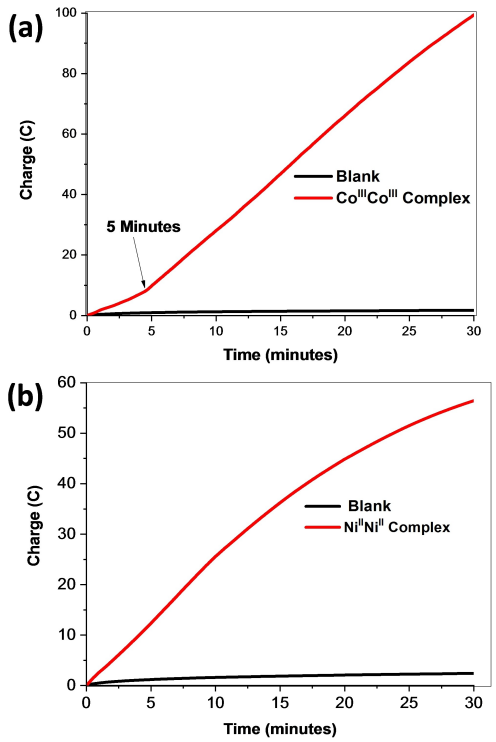

Figure 4. Plot of charge vs. time for electrocatalytic H_2 generation. (a) **1**, (b) 2 (CV/BE): Hg-pool; Ag/AgCl; Pt wire/coil; phosphate buffer (pH 7); AP: −1.6 $V_{Ag/AgCl}$ (BE)

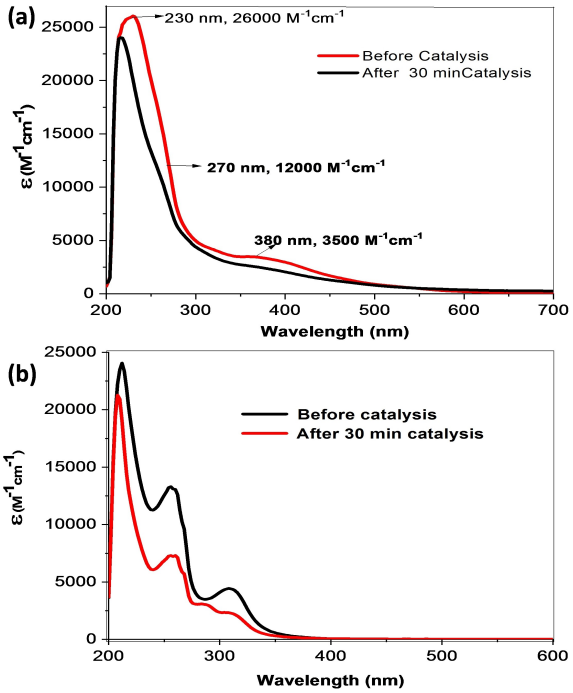

Figure 6. Comparison of the UV-Visible before and after bulk-electrolysis (BE) of a. **1**, and b. **2** at −1.6 VAg/AgCl with water (Hg pool: WE, Pt coil: AE, Ag/AgCl: RE, phosphate buffer at pH 7).

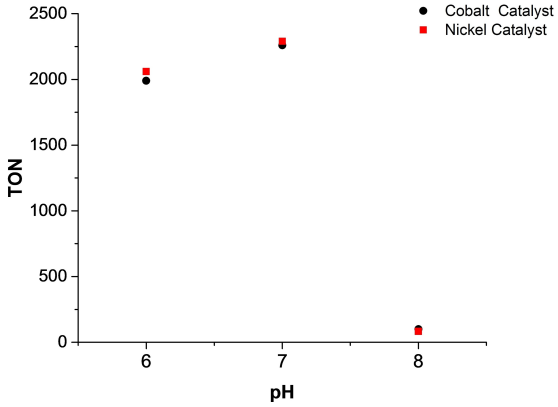

Figure 5. Variation of TON with pH.

Post-catalytic analysis

The fate of catalysts **1** and **2** was analyzed by comparison of their electronic spectra before and after 30-minute catalysis, as shown in Figure 6. Both catalysts seem to retain most of their characteristics, suggesting that the operative water reduction catalysts are molecular in nature.

For catalyst **1** there is a slight but noticeable reduction of the processes at 230 nm and 270 nm (sh). As these are π–π* processes, this is indicative of stress or distortion of the ligand framework, possibly associated with bond breaking. In fact, the broad peak at ca. 380 nm and 435 nm (sh) flattens. In order to assess experimentally the nature of this peak we acquired the spectrum of an acetonitrile solution containing the salt cobalt (II) perchlorate and pyrazole (Figure S21). The decrease in bands in the post-catalytic product suggests that at least one of the pyrazole units is either partially coordinated or completely removed. If the latter, this is likely a mechanism of deactivation. Figure S21 shows a decrease in the 217 nm and 248 nm bands, which are associated with Co^{III}←$N_{pyrazole}$ charge transfer transition (LMCT) peak at 370 nm. For **2**, the processes at 212 and 257 (shoulder) nm assigned to π–π* transitions, are decreased. The band at 212 nm decreases and shifts to ~207 nm, while the one at 257 nm reduces ~50%. The band at 310 nm is attributed to phenolate←Ni ^{II} charge transfer transition (MLCT) and splits in two bands at 288 nm and 310 nm.[37] The possibility of the formation of nanoparticles was studied by bulk electrolysis in phosphate buffer (1 M, pH 7) using grafoil® as the working electrode comparatively in the presence and in the absence of species **1** and **2** for 15, 30 and 60 minutes. Scanning electron microscopy (SEM) images of the electrodes are shown in Figure 7 and consistently show the absence of any material deposited onto the electrodes of the blank (Figures 7a, d, g).

The Co_2-containing **1** shows comparably clean electrodes without obvious material or nanoparticle depositions (Figures 7b, e, h). This is indicative of molecular activity in **1**. This species withstands up to 1 h bulk electrolysis. However, deposition of solid particles was observed for the Ni_2-containing **2** after 30 and 60 minutes (Figures 7c, f, i). Energy dispersive spectroscopic (EDS) analysis indicated that the metal content on that material was below the detectable limits (Table T3–

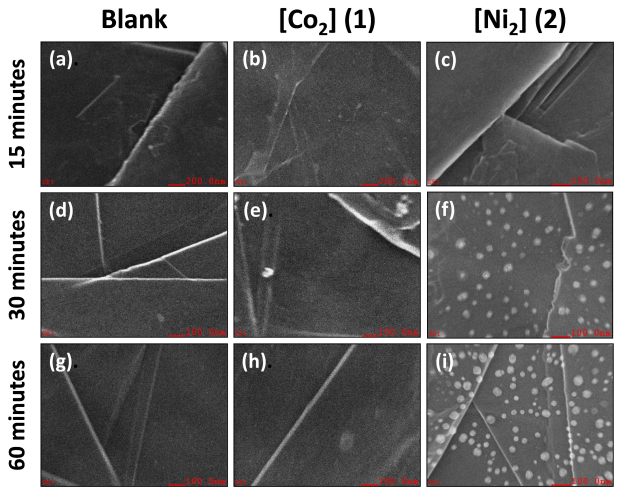

Figure 7. SEM images of grafoil electrodes for **1** and **2** after bulk electrolysis in phosphate buffer (1 M, pH 7) at −1.6 V. Red scalebar 200 nm (a, b); 100 nm (c–i).

Table T8) and that the nanoparticulates are organic in nature. Because these agglomerates cannot sustain catalysis, and H_2 generation happens prior to the formation of solids, the catalytic activity of **2** is also ascribed as molecular in nature. However, catalyst **2** does not seem to withstand the hardship of the process as well as **1**.

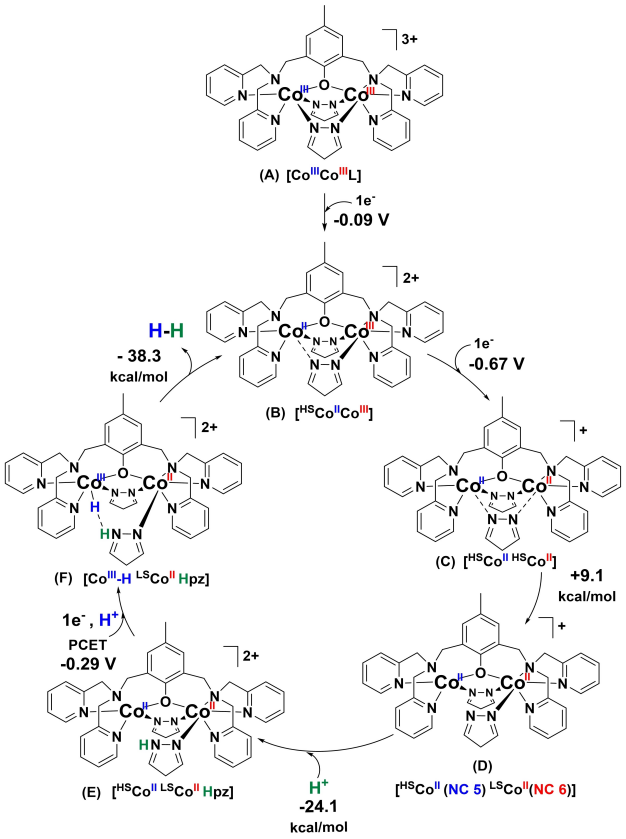

Figure 8. Catalytic mechanism of H_2 generation by **1** in phosphate buffer at pH 7

Discussion of proposed catalytic routes

The above-described experimental results support the involvement of species **1** and **2** in molecular electrocatalytic water reduction. These results prompted the use of DFT methodology to make a concerted analysis and propose energetically favorable mechanisms for the global process.

The electrocatalytic pathways taken by compound **1** were modelled as starting with a procatalyst **A** containing two six-coordinated and low spin $3d^6$ Co^{III} centers each bound to two pyridines and one amine and bridged by the phenolate of ligand L and two pyrazolate co-ligands. The calculated geometry, redox states and electronic configurations are in full agreement with structural data in the solid and in solution. Figure 8 summarizes the findings. Species A undergoes a one-electron reduction at a calculated potential of $-0.09\ V_{Fc/Fc+}$ to yield species **B**. The calculated potential is in good agreement with the experimental value $-0.12\ V_{Fc/Fc+}$ ($0.28\ V_{Ag/AgCl}$). Species **B** contains a high-spin $3d^7$ Co^{II} and a low spin Co^{III} leading to local asymmetry imposed by a longer Co^{II}-pyrazole bond. Further reduction of **B** by one electron at a calculated potential of $-0.67\ V_{Fc/Fc+}$, yielding species **C**, in reasonable agreement ($\Delta E < 20$ mV) with the experimental value of $-0.49\ V_{Fc/Fc+}$ ($-0.09\ V_{Ag/AgCl}$). Species **C** contains two high spin $3d^7$ Co^{II} centers that are considerably more labile than their initial $^{LS}3d^6$ counterparts. As previously discussed, the distance of the two Co centers in **1** was measured by X-ray crystallography at 3.183 Å, thus shorter than in other similar Co_2 species[21] and in the Ni–Ni and Zn–Zn distance observed for **2** and **3**. In order to release the tension of the core one Co^{II}-pyrazole bond breaks off with an energy of +9.1 kcal/mol and triggers an electronic redistribution in which the resulting five coordinate Co^{II} remains $^{HS}3d^7$ with S = 3/2, while the other Co^{II} responds to the stronger six-coordination becoming a low-spin $3d^7$ ion with S = 1/2. This isolated step is slightly unfavorable and makes sense from a global perspective of enabling other favorable steps towards H_2 release. This [$^{HS}Co^{II}$ $^{LS}Co^{II}$Pz] species **D** captures a H^+ resulting in the protonation of the pyrazolate bound to the $^{LS}Co^{II}$ and forming species **E**. This protonation is favored by −24 kcal/mol and enables a proton-coupled electron transfer (PCET) in which one electron and one proton are transferred at −0.29 V to the five-coordinate $^{HS}Co^{II}$ yielding species **F**. This species contains a $^{LS}Co^{III}$-H hydride species, considered indispensable for catalytic activity, that is spatially and geometrically close to the protonated pyrazole allowing for a relay mechanism similar to that recently proposed for a copper catalyst.[15c] The combination of hydride and proton yields H_2 that is favorably released with an energy of −38.3 kcal/mol, regenerating the initial species **B**.

This mechanism, although energetically favorable and effective, differs from that proposed for another bimetallic Co^{III} species recently described by our group.[9] In that case an amido-bridged framework brought electronic cooperativity in which both cobalt centers share the burden of catalysis by

being in close distance, with favorable topology and orientation/overlap of the redox-active orbitals. The cooperativity observed for **1** is structural in nature, in which one cobalt center adapts in order to favor the activity by the neighboring center; however, the electronic contribution of these centers to the catalytic process is not equivalent. This structural cooperativity also differs from the behavior reported for another pyrazolato-based system described by Nam, Llobet, Fukuzumi et al.[14b] in which the centers are 3.95 Å apart and behave independently.

The proposed catalytic route for the Ni-containing **2** is complicated by irreversible electrochemistry, and a fragile structure that degrades over the catalytic cycle. The species was modelled with two $^{HS}3d^8$ Ni^{II} centers, starting with a pro-catalytic species **G** that can undergo a series of competing PCET processes shown in Figure 9. The first possible PCET requires -1.40 $V_{Fc/Fc+}$ and involves the reduction of one pyridine ring forming a reactive pyridinium radical in species **K**, likely associated with demetallation and decomposition observed by SEM. The second possible process involves a $2e^-$:$1H^+$ PCET at -1.55 $V_{Fc/Fc+}$ along with chloride loss to form the $3d^7$ Ni^{II}-H hydride species **I** that favorably reacts with H+ (-35 kcal/mol) to form species **J** with 5-coordinate and 6-coordinate Ni^{II} centers upon elimination of H_2. Upon PCET at -1.33 $V_{Fc/Fc+}$ **J** yields species **H** that contains a $3d^6$ Ni^{III}-H hydride that can be converted to **I**, continuing the catalytic cycle. Alternatively, the initial species **G** can form **H** via a $1e^-$:$1H^+$ PCET at -2.79 $V_{Fc/Fc+}$. The involvement of multiple PCET processes in the presence of acid requires potentials different from those experimentally observed in acetonitrile at -0.52 $V_{Fc/Fc+}$ (-0.13 $V_{Ag/AgCl}$) for $Ni^{II}Ni^{II} \rightarrow Ni^{II}Ni^{I}$ and at -1.79 $V_{Fc/Fc+}$ (-1.40 $V_{Ag/AgCl}$) for a nominal $Ni^{II}Ni^{II} \rightarrow Ni^{I}Ni^{I}$ that likely requires ligand reduction and illustrates the complexity of catalyst deactivation mechanisms. No obvious cooperative effect was observed.

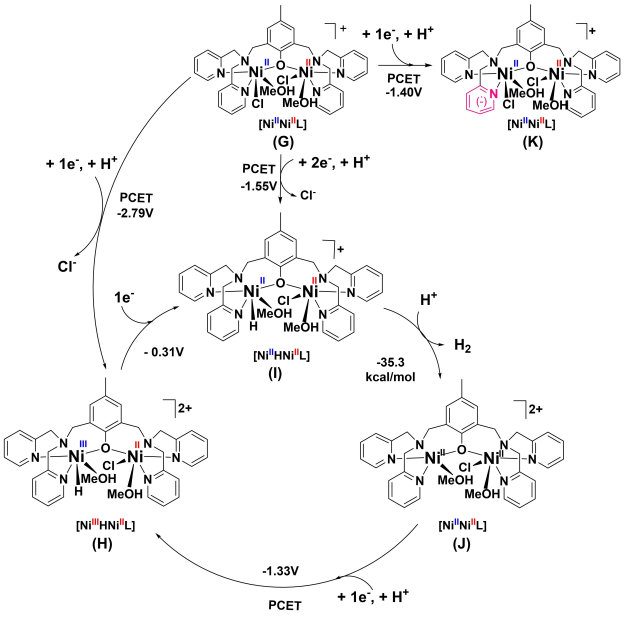

Figure 9. Catalytic mechanism of H_2 generation by **2** in phosphate

Summary and Conclusions

In this paper we have investigated by means of experimental and DFT methods the $3d^6$ species $[LCo^{III}_2(\mu\text{-}Pz)_2](ClO_4)_3$ (**1**), the $3d^8$ species $[LNi^{II}_2(CH_3OH)_2Cl_2]ClO_4$ (**2**), and the $3d^{10}$ species $[LZn^{II}_2Cl_2]PF_6$ (**3**) supported by the deprotonated form of 2,6-bis[bis(2-pyridylmethyl) aminomethyl]-4-methylphenol. This ligand was a staple of bioinorganic modelling in the 1990s and was selected because it imposes close proximity to two neighboring 3d metal centers in similar coordination environments. The structures of **1**, **2**, and **3** were meticulously established by crystallographic and 2D NMR methods and these species were probed as catalysts for water reduction. As expected, species **3** containing redox-inactive $3d^{10}$ Zn^{II} ions is not active and allowed us to rule out ligand-based catalysis. The cobalt containing **1** and the nickel-containing **2** are catalytic towards water reduction, although they rely on distinct pathways to produce H_2. The cobalt catalyst **1** starts as a triply bridged $3d^6$ $[^{LS}Co^{III}(\mu\text{-}PhO)(\mu\text{-}Pz)_2{}^{LS}Co^{III}]$ procatalyst that is initially reduced to $3d^6$-$3d^7$ $[^{LS}Co^{III}\ {}^{HS}Co^{II}]$ and then to $[^{HS}Co^{II}\ {}^{HS}Co^{II}]$. The presence of two labile $3d^7$ ions leads to the rupture of one Co-N_{Pz} bond and further electronic redistribution that results in a five-coordinate $^{HS}Co^{II}$ and a six-coordinate $^{LS}Co^{II}$. This step is crucial for catalysis, as it opens the coordination sphere of at least one metal center. This nucleophilic $[^{HS}Co^{II}\ {}^{LS}Co^{II}Pz]$ attacks a proton, but rather than hydride formation, pyrazolate protonation is favored and takes place. A favorable PCET step leads to the formation of a $[^{LS}Co^{III}$-H $^{LS}Co^{II}PzH]$ hydride. The hydride and the PzH are spatially and geometrically close to each other to form H_2. Post-catalytic analysis supports the molecular nature of **1**. This cooperativity is predominantly structural, although as described by Papanikolaou et al.[11] the observed HS/LS spin switch may modulate the reactivity of the catalytic Co^{II} site and add an electronic component to cooperativity. The nickel-containing **2**, on the other hand, presents several competing PCET pathways. These processes can lead to the formation of a reactive pyridinium radical prone to catalyst deactivation or to a $3d^7$ Ni^{II}-H hydride species in a step that involves two electrons and one proton. Another multielectronic PCET process at high potentials leads to a $3d^6$ Ni^{III}-H. None of these pathways seems to display metal cooperativity; however, the deposition of organic matter to the electrode suggests that catalyst deactivation takes place. These results, allied to our previous work,[9] point out to the distinction between electronic and structural cooperativity and their relationship to the coordination environment and the nature of the metal centers. Future studies will interrogate cooperativity in both homo- and hetero-nuclear systems.

Experimental Section

Experimental Details

General

Solvents and reagents were used as received from commercial sources. ^{1}H NMR spectroscopy was attained with an NMR MR 400 MHz. MR 400 MHz setup using $CDCl_3$ and CD_3CN as solvents, and elemental analysis was performed by Midwest Microlab, using an Exeter CHN analyzer. Micromass ZQLC/MS equipment was used to obtain mass spectra and Fourier transform infrared (FTIR) spectra of the ligand and complexes were obtained as KBr pellets on a Brucker Tensor 27 FTIR spectrometer scanning from 4,000 to 600 cm^{-1}. A UV-3600 Shimadzu spectrophotometer operating within a range of 190 to 1,600 nm with quartz cells at room temperature was used to record UV-visible spectra of ligand and complexes.

Electrochemistry

The electrochemical behavior of compounds **1**–**3** was studied with a BAS 50 W potentiostat/galvanostat. Cyclic voltammograms of the compounds were measured in acetonitrile using $TBAPF_6$ as a supporting electrolyte and ferrocene/ferrocenium (Fc/Fc^+) as an internal standard.[27] Cyclic voltammograms were run at room temperature under inert conditions in an electrochemical cell containing a glassy carbon working electrode, auxiliary platinum wire, and reference Ag^+/AgCl electrode. To evaluate the reversibility of the redox processes, the peak-peak potential separations, ($\Delta Ep = |E_{p,c}\text{-}E_{p,a}|$) and $|i_{pa}/i_{pc}|$ were calculated.

Water Reduction Catalysis

To analyze the catalytic activity of **1** and **2**, CV experiments were performed in aqueous phosphate buffer at pH of 7, using a working mercury pool electrode. Bulk electrolysis was used to quantify the amount of H_2 generated in phosphate buffer (1 M, pH 7) using Hg-pool as working electrode, Ag/AgCl as reference electrode and a platinum wire as auxiliary electrode. A custom-made H-type cell with two compartments of dissimilar volume separated by a frit was used for the bulk electrolysis experiment. The larger compartment houses the working and reference electrodes, while the small compartment houses the auxiliary electrode.

Scanning Electron Microscope (SEM) Analysis and Energy Dispersive Spectroscopy (EDS)

Confirmation of the molecular nature of catalysts **1** and **2** were assessed by running a bulk electrolysis experiment with identical conditions as water reduction except for the Hg-pool electrode which is changed to a conducting grafoil electrode. After bulk electrolysis, SEM images were obtained for the grafoil electrode and EDS was used to identify specific elements in the SEM as well as determining their relative proportions. Species **1** showed no visible particles on the SEM, whereas **2** showed solid particles in the SEM even though the EDS analysis indicated that metal content was below detectable limits.

X-ray Crystal Determination

Dark brown rod-like crystals of dimensions, 0.556 mm × 0.558 mm × 0.446 mm were obtained for **1** through recrystallization in acetonitrile: isopropanol (4 : 1). **2** gave light green plate-like crystals with dimensions, 0.350 mm × 0.427 mm × 0.457 mm and **3** gave clear rod-like crystals with dimensions, 0.570 mm × 0.460 mm × 0.230 mm via slow evaporation in methanol. These crystals were mounted on a mitogen loop with paratone oil. Crystallographic data was collected with a Bruker APEX-II Kappa geometry diffractometer with Mo radiation and a graphite monochromator using a Bruker charge coupled device (CCD) based diffractometer equipped with an Oxford Cryostream low temperature apparatus. All data were collected at 100 K with omega and phi scans of 0.5° per frame for 30s. All the structures were solved by direct methods using SHELXS-97 program which is part of APEX II and refined by least squares method on F^2 using SHELXL on OLEX 2. The structure of **1** and **3** were solved in space group $P\bar{1}$ whereas **2** was solved in space group $P2_1/n$. Compounds **1** and **2** consist of one cationic molecule in the asymmetric unit cell with three perchlorate counterions and one perchlorate counterions respectively. **3** consists of two cationic molecules in the asymmetric unit cell with one hexafluorophosphate counterion molecule per cationic molecule.

Deposition Numbers 2112779 (**1**), 2112780 (**2**) and 2112778 (**3**) contain the supplementary crystallographic data for this paper. These data are provided free of charge by the joint Cambridge Crystallographic Data Centre and Fachinformationszentrum Karlsruhe Access Structures service.

DFT Calculations

Unrestricted Kohn–Sham density functional theory (UKS-DFT) calculations were performed with the Gaussian 16 quantum chemical program package[38] using the hybrid exchange-correlation functional B3LYP.[39] Ahlrich's def2-SVP basis set[40] was utilized for geometry optimizations and vibrational mode calculations. The SMD continuum solvation method[41] was used to estimate the free energy of solvation in MeCN ($\varepsilon = 35.688$). Grimme's D3 corrections were applied with Becke–Johnson damping [42] to account for dispersion forces which are known to be otherwise deficient in B3LYP. Accurate free energies were obtained by performing single point calculations with the def2-TZVPP basis set[43] using the def2-SVP optimized structures, zero-point energies and thermal corrections (See Supporting Information for details).

Synthetic Procedures

2,6-Bis[(bis(2-pyridylmethyl)amino)methyl]-4-methylphenol (HL): The ligand HL was synthesized and characterized by reported procedures.[19]

$[LCo_2(\mu\text{-}Pz)_2](ClO_4)_3$ (1): Synthesis of this complex was done by a modification of a procedure reported in the literature[44] (Figure S2). To a solution of **HL** (0.226 g, 0.43 mmol) in methanol (10 mL), a solution of $Co(ClO_4)_2{\cdot}6H_2O$ (0.311 g, 0.85 mmol) in methanol (10 mL) was added dropwise while stirring. This solution was then treated with a solution of pyrazole in methanol (HPz) (0.014 g, 0.20 mmol) and the resulting solution was heated on a steam-bath for 5–10 min. The resulting solution was filtered while hot through celite and then allowed to crystallize by slow evaporation at room temperature. Dark brown microcrystals were formed after 2 days and recrystallized with acetonitrile and 2.5 mL of isopropanol to yield X-ray quality crystals. The crystals were washed with diethyl ether and isopropanol and dried at room temperature under vacuum. Yield = 68 % ^{1}H NMR [500 MHz, CD_3CN, 300 K] δ/ppm =) 2.03 (s, 3 H, Methyl), 3.42 (d, 2H, CH_2), 3.64 (d, 2H, CH_2) 4.27 (s, 4 H, CH_2), 4.50 (d, 2 H, CH_2), 5.17 (d, 2 H, CH_2), 6.67 (s, 4 H, PyH), 6.85 (s, 2 H, PyH), 6.99 (d, 2H, ArH), 7.76 (m, 4H, pzH), 8.01 (m, 2 H, pyH), 8.20 (m, 2 H, pyH), 8.31 (m, 2 H, pyH), 8.58 (s, 2 H, pyH), 8.81 (s, 2H, pyH); ESI/MS in CH_3CN: m/z + = 260.55; IR (KBr, cm^{-1}): 3423(w), (O–H

stretch); 1611(s), 1480(s), 1437(s), 1387(s), 1288(s) (C=C ring stretch); 1089(sh) (Cl–O). Elemental Analysis Calculated for $C_{39}H_{41}Cl_3Co_2N_{10}O_{14}$: C, 42.66; H, 3.76; N, 12.76. Found: C, 42.38; H, 3.65; N, 12.35.

$[LNi_2(CH_3OH)_2Cl_2]ClO_4$ (**2**): This complex was synthesized by a slight modification of a reported procedure in the literature[18b] (Figure S2). To a solution of **HL** (0.265 g, 0.50 mmol) in methanol (10 mL), a solution of $NiCl_2 \cdot 6H_2O$ (0.238 g, 1.00 mmol) in methanol (10 mL) was added dropwise while stirring. This solution was then treated with a solution of $NaClO_4$ (0.184 g, 1.50 mmol) and the resulting solution was heated on a steam-bath for 5–10 min. The resulting solution was filtered while hot through celite and then allowed to crystallize by slow evaporation at room temperature. Light bluish-green X-ray quality crystals were formed after 2 days. Crystals were washed with diethyl ether and isopropanol and dried at room temperature. Yield = 70% ESI/MS in CH_3CN: m/z + = 716.98; IR (KBr, cm^{-1}): 3245(w), (O–H stretch); 1607(s), 1474(s), (C=C ring stretch); 1096(sh) (Cl–O). Elemental Analysis Calculated for $C_{36}H_{47}Cl_3N_6Ni_2O_9$: C, 46.42; H, 5.09; N, 9.05. Found: C, 46.28; H, 5.14; N, 9.16.

$[LZn_2Cl_2]PF_6$ (**3**): This complex was synthesized by a slight modification of a reported procedure in the literature[18b] (Figure S2). To a solution of **HL** (0.141 g, 0.27 mmol) in methanol (10 mL), a solution of $ZnCl_2 \cdot 6H_2O$ (0.073 g, 0.53 mmol) in methanol (10 mL) was added dropwise while stirring. This solution was then treated with a solution of NH_4PF_6 (0.245 g, 1.50 mmol) and the resulting solution was heated on a steam-bath for 5–10 min. The resulting solution was filtered through celite and then allowed to crystallize by slow evaporation at room temperature. Long colorless X-ray quality crystals were formed after 2 days. Crystals were washed with diethyl ether and isopropanol and dried at room temperature Yield = 75%; ^{1}H NMR [500 MHz, CD_2Cl_2, 300 K] δ/ppm =) 1.97 (s, 3 H, Methyl), 3.52 (d, 2H, CH_2), 3.81 (d, 2H, CH_2) 3.89 (d, 2H, CH_2), 4.15 (d, 2 H, CH_2), 4.46 (m, 4 H, CH_2), 6.60 (d, 2H, ArH), 7.15 (s, 2 H, PyH), 7.22 (s, 2H, PyH), 7.53(s, 2H, PyH), 7.64 (s, 2H, PyH), 7.72 (s, 2H, PyH), 8.06 (m, 2 H, pyH), 8.80 (s, 2 H, pyH), 9.33 (s, 2H, pyH); ESI/MS in CH_3CN: m/z + = 748.81; IR (KBr, cm^{-1}): 3423(w), (O–H stretch); 1611(s), 1480(s), 1437(s), 1387(s), 1288(s) (C=C ring stretch); 1089(sh) (Cl–O). Elemental Analysis Calculated for $C_{33}H_{35}Cl_2F_6N_6O_2Zn_2$: C, 44.32; H, 3.94; N, 9.40. Found: C, 44.19; H, 3.78; N, 9.51.

Acknowledgements

C.N.V. and H.B.S. acknowledge support from the U.S. Department of Energy (DOE-BES) through the grants DE-SC0001907 and DE-FG02-09ER16120. Further support is acknowledged through the U.S. Department of Energy (DOE-BES DE-FOA0002414) for C.N.V. and U.S National Science Foundation (NSF grant CHE1856437) to H.B.S. The authors acknowledge the WSU-Computing Grid for access to their facilities.

Conflict of Interest

The authors declare no conflict of interest.

Data Availability Statement

The data that support the findings of this study are available in the supplementary material of this article.

Keywords: bimetallic cooperativity · cobalt catalysts · nickel catalysts · proton reduction · water reduction · zinc complexes

[1] a) L. Tong, L. Duan, A. Zhou, R. P. Thummel, *Coord. Chem. Rev.* **2020**, *402*, 213079; b) R. M. Bullock, A. M. Appel, M. L. Helm, *Chem. Commun.* **2014**, *50*, 3125–3143; c) V. S. Thoi, Y. Sun, J. R. Long, C. J. Chang, *Chem. Soc. Rev.* **2013**, *42*, 2388–2400; d) L. Tong, A. Iwase, A. Nattestad, U. Bach, M. Weidelener, G. Götz, A. Mishra, P. Bäuerle, R. Amal, G. G. Wallace, *Energy Environ. Sci.* **2012**, *5*, 9472–9475.
[2] H. Baydoun, S. Mazumder, H. B. Schlegel, C. N. Verani, *Chem. Eur. J.* **2017**, *23*, 9266–9271.
[3] a) W. Kang, C. C. Lee, A. J. Jasniewski, M. W. Ribbe, Y. Hu, *Sci. J.* **2020**, *368*, 1381–1385; b) A. Sekretaryova, S. M. Jones, E. I. Solomon, *J. Am. Chem. Soc.* **2019**, *141*, 11304–11314; c) B. M. Hoffman, D. Lukoyanov, Z. Y. Yang, D. R. Dean, L. C. Seefeldt, *Chem. Rev.* **2014**, *114*, 4041–4062; d) R. L. Hollingsworth, J. W. Beattie, A. Grass, P. D. Martin, S. Groysman, R. L. Lord, *Dalton Trans.* **2018**, *47*, 15353–15363; e) N. Sträter, W. Lipscomb, T. Klabunde, B. Krebs, *Angew. Chem. Int. Ed.* **1996**, *35*, 2024–2055; *Angew. Chem.* **1996**, *108*, 2158–2191; f) S. Tschierlei, S. Ott, R. Lomoth, *Energy Environ. Sci.* **2011**, *4*, 2340–2352; g) A. Neves, M. Lanznaster, A. J. Bortoluzzi, R. A. Peralta, A. Casellato, E. E. Castellano, P. Herrald, M. J. Riley, G. Schenk, *J. Am. Chem. Soc.* **2007**, *129*, 7486–7487.
[4] a) Q. Wang, S. H. Brooks, T. Liu, N. C. Tomson, *Chem. Commun.* **2021**, *57*, 2839–2853; b) B. D. Nath, K. Takaishi, T. Ema *Catal. Sci. Technol.* **2020**, *10*, 12–34; c) D. G. Hetterscheid, S. H. Chikkali, B. de Bruin, J. N. Reek, *ChemCatChem* **2013**, *5*, 2785–2793; d) J. P. McInnis, M. Delferro, T. J. Marks, *Acc. Chem. Res.* **2014**, *47*, 2545–2557.
[5] S. Kal, A. S. Filatov, P. H. Dinolfo, *Inorg. Chem.* **2014**, *53*, 7137–7145.
[6] a) N. Pilkington, R. Robson, *Aust. J. Chem.* **1970**, *23*, 2225–2236; b) H. Ōkawa, H. Furutachi, D. E. Fenton, *Coord. Chem. Rev.* **1998**, *174*, 51–75.
[7] T. LeBlond, P. H. Dinolfo, *Inorg. Chem.* **2020**, *59*, 3764–3774.
[8] P. Tong, W. Xie, D. Yang, B. Wang, X. Ji, J. Li, J. Qu, *Dalton Trans.* **2016**, *45*, 18559–18565.
[9] K. K. Kpogo, S. Mazumder, D. Wang, H. B. Schlegel, A. T. Fiedler, C. N. Verani, *Chem. Eur. J.* **2017**, *23*, 9272–9279.
[10] S. K. Padhi, S. Rai, S. S. Akhter, *Inorg. Chem.* **2020**, *59*, 7810–7821.
[11] M. G. Papanikolaou, A. Elliott, J. McAllister, J. K. Gallos, A. D. Keramidas, T. A. Kabanos, S. Sproules, H. N. Miras, *Dalton Trans.* **2020**, *49*, 15718–15730.
[12] T. Hamaguchi, K. Kai, I. Ando, K. Kawano, K. Yamauchi, K. Sakai, *Inorg. Chim. Acta* **2020**, *505*, 119498.
[13] a) C. N. Valdez, J. L. Dempsey, B. S. Brunschwig, J. R. Winkler, H. B. Gray, *PNAS* **2012**, *109*, 15589–15593; b) S. M. Laga, J. D. Blakemore, L. M. Henling, B. S. Brunschwig, H. B. Gray, *Inorg. Chem.* **2014**, *53*, 12668–12670.
[14] a) C. Di Giovanni, C. Gimbert-Suriñach, M. Nippe, J. Benet-Buchholz, J. R. Long, X. Sala, A. Llobet, *Chem. Eur. J.* **2016**, *22*, 361–369; b) S. Mandal, S. Shikano, Y. Yamada, Y. M. Lee, W. Nam, A. Llobet, S. Fukuzumi, *J. Am. Chem. Soc.* **2013**, *135* (41), 15294–15297.
[15] a) N. El Harakeh, A. de Morais, N. Rani, J. Gomez, A. Cousino, M. Lanznaster, S. Mazumder, C. Verani, *Angew. Chem. Int. Ed.* **2021**, *60*, 5723–5728; *Angew. Chem.* **2021**, *133*, 5787–5792; b) P. H. Kankanamalage, D. M. Ekanayake, N. Singh, A. C. de Morais, S. Mazumder, C. N. Verani, A. Mukherjee, M. Lanznaster, *New J. Chem.* **2019**, *43*, 12795–12803; c) D. M. Ekanayake, K. M. Kulesa, J. Singh, K. K. Kpogo, S. Mazumder, H. B. Schlegel, C. N. Verani, *Dalton Trans.* **2017**, *46*, 16812–16820; d) P. H. A. Kankanamalage, S. Mazumder, V. Tiwari, K. K. Kpogo, H. B. Schlegel, C. N. Verani, *Chem. Commun.* **2016**, *52*, 13357–13360; e) D. Basu, S. Mazumder, X. Shi, R. Staples, H. Schlegel, C. Verani, *Angew. Chem. Int. Ed.* **2015**, *54*, 7139–7143; *Angew. Chem.* **2015**, *127*, 7245–7249; f) D. Basu, S. Mazumder, X. Shi, H. Baydoun, J. Niklas, O. Poluektov, H. Schlegel, C. Verani, *Angew. Chem. Int. Ed.* **2015**, *54*, 2105–2110; *Angew. Chem.* **2015**, *127*, 2133–2138.
[16] G. Anderegg, F. Wenk, *Helv. Chim. Acta* **1967**, *50*, 2330–2332.
[17] S. Masatatsu, K. Hajime, M. Ichiro, *Chem. Lett.* **1981**, *10*, 1745–1748.
[18] a) A. Neves, M. A. de Brito, I. Vencato, V. Drago, K. Griesar, W. Haase, *Inorg. Chem.* **1996**, *35*, 2360–2368; b) S. S. Massoud, M. Spell, C. C. Ledet,

T. Junk, R. Herchel, R. C. Fischer, Z. Trávníček, F. A. Mautner, *Dalton Trans.* **2015**, *44*, 2110–2121.
[19] A. S. Borovik, V. P. Lucille, F. Taylor, P. O. Anderson, L. J. Que, *J. Am. Chem. Soc.* **1989**, *111*, 6183–6195.
[20] R. Alizadeh, N. Ghazinia, *Advanc. J. Chem. A* **2019**, *2*, 184–189.
[21] J. S. Seo, R. C. Hynes, D. Williams, J. Chin, N. D. Sung, *J. Am. Chem. Soc.* **1998**, *120* (38), 9943–9944.
[22] F. B. Johansson, A. D. Bond, U. G. Nielsen, B. Moubaraki, K. S. Murray, K. J. Berry, J. A. Larrabee, C. J. McKenzie *Inorg. Chem.* **2008**, *47*, 5079–5092.
[23] S. Bosch, P. Comba, L. R. Gahan, G. Schenk, *Inorg. Chem.* **2014**, *53*, 9036–9051.
[24] W. P. Aue, E. Bartholdi, R. R. Ernst, *J. Chem. Phys.* **1976**, *64*, 2229–2246.
[25] F. C. Nachod, *Determination Of Organic Structures By Physical Methods*; Vol. Volume 6 Physics.
[26] G. W. Vuister, A. D. Bax, *J. Magn. Reson. 98*, 428–435.
[27] R. R. Gagne, C. A. Koval, G. C. Lisensky, *Inorg. Chem.* **1980**, *19*, 2854–2855.
[28] a) R. Shakya, C. Imbert, H. P. Hratchian, M. Lanznaster, M. J. Heeg, B. R. McGarvey, M. Allard, H. B. Schlegel, C. N. Verani, *Dalton Trans.* **2006**, 2517–2525; b) D. Basu, M. M. Allard, F. R. Xavier, M. J. Heeg, H. B. Schlegel, C. N. Verani, *Dalton Trans.* **2015**, *44*, 3454–3466; c) H. Wang, E. Mijangos, S. Ott, A. Thapper, *Angew. Chem. Int. Ed.* **2014**, *53*, 14499–14502; *Angew. Chem.* **2014**, *126*, 14727–14730.
[29] C. C. V. Chaves, G. Farias, M. D. Formagio, A. Neves, R. M. Peralta, J. M. G. Mikcha, B. de Souza, R. A. Peralta, *Inorg. Chim. Acta* **2020**, *507*, 119559.
[30] A. K. Barik, S. Paul, R. J. Butcher, S. K. Kar, *Polyhedron* **2000**, *19*, 2651–2655.
[31] M. M. Allard, F. R. Xavier, M. J. Heeg, H. B. Schlegel, C. N. Verani, *Eur. J. Inorg. Chem.* **2012**, *2012*, 4622–4631.
[32] S. Mukhopadhyay, D. Mandal, D. Ghosh, I. Goldberg, M. Chaudhury, *Inorg. Chem.* **2003**, *42*, 8439–8445.
[33] O. Rotthaus, F. Thomas, O. Jarjayes, C. Philouze, E. Saint-Aman, J. L. Pierre, *Chem. Eur. J.* **2006**, *12*, 6953–6962.
[34] O. Rotthaus, O. Jarjayes, F. Thomas, C. Philouze, C. Perez Del Valle, E. Saint-Aman, J. L. Pierre, *Chem. Eur. J.* **2006**, *12*, 2293–2302.
[35] T. R. Holman, M. P. Hendrich, L. Que Jr, *Inorg. Chem.* **1992**, 937–939.
[36] V. Fourmond, P. A. Jacques, M. Fontecave, V. Artero, *Inorg. Chem.* **2010**, *49*, 10338–10347.
[37] M. Wang, L. Chen, L. Sun, *Energy Environ. Sci.* **2012**, *5*, 6763–6778.
[38] M. J. Frisch, G. W. Trucks, H. B. Schlegel, G. E. Scuseria, M. A. Robb, J. R. Cheeseman, G. Scalmani, V. Barone, G. A. Petersson, H. Nakatsuji, X. Li, M. Caricato, A. V. Marenich, J. Bloino, B. G. Janesko, R. Gomperts, B. Mennucci, H. P. Hratchian, J. V. Ortiz, A. F. Izmaylov, J. L. Sonnenberg, W. F. Ding, F. Lipparini, F. Egidi, J. Goings, B. Peng, A. Petrone, T. Henderson, D. Ranasinghe, V. G. Zakrzewski, J. Gao, N. Rega, G. Zheng, W. Liang, M. Hada, M. Ehara, K. Toyota, R. Fukuda, J. Hasegawa, M. Ishida, T. Nakajima, Y. Honda, O. Kitao, H. Nakai, T. Vreven, K. Throssell, J. A. Montgomery Jr., J. E. Peralta, F. Ogliaro, M. J. Bearpark, J. J. Heyd, E. N. Brothers, K. N. Kudin, V. N. Staroverov, T. A. Keith, R. Kobayashi, J. Normand, K. Raghavachari, A. P. Rendell, J. C. Burant, S. S. Iyengar, J. Tomasi, M. Cossi, J. M. Millam, M. M. Klene, C. Adamo, R. Cammi, J. W. Ochterski, R. L. Martin, K. Morokuma, O. Farkas, J. B. Foresman, D. J. Fox, *Gaussian 16, rev C. 01*, Wallingford, CT, **2016**.
[39] a) A. D. Becke, *Phys. Rev. A* **1988**, *38*, 3098; b) C. Lee, W. Yang, R. G. Parr, *Phys. Rev. B* **1988**, *37*, 785; c) A. D. Becke, *J. Chem. Phys.* **1993**, *98*, 5648.
[40] A. Schäfer, H. Horn, R. Ahlrichs, *J. Chem. Phys.* **1992**, *97*, 2571–2577.
[41] A. V. Marenich, C. J. Cramer, D. G. Truhlar, *J. Phys. Chem.* **2009**, *113*, 6378–6396.
[42] a) S. Grimme, *J. Comb. Chem.* **2006**, *27*, 1787–1799; b) S. Grimme, J. Antony, S. Ehrlich, H. Krieg, *J. Chem. Phys.* **2010**, *132*, 154104; c) S. Grimme, S. Ehrlich, L. Goerigk, *J. Comb. Chem.* **2011**, *32*, 1456–1465.
[43] a) A. Schäfer, C. Huber, R. Ahlrichs, *J. Chem. Phys.* **1994**, *100*, 5829–5835; b) F. Weigend, R. Ahlrichs, *Phys. Chem. Chem. Phys.* **2005**, *7*, 3297–3305.
[44] S. S. Massoud, T. Junk, F. R. Louka, R. Herchel, Z. Trávníček, R. C. Fischer, F. A. Mautner, *RSC Adv.* **2015**, *5*, 87139–87150.

Manuscript received: December 14, 2021
Accepted manuscript online: February 25, 2022
Version of record online: March 19, 2022